Electron-scale turbulence spectra and plasma thermal transport responding to continuous $E \times B$ shear ramp-up in a spherical tokamak

2013 Nucl. Fusion 53 083007

(http://iopscience.iop.org/0029-5515/53/8/083007)

IOP Publishing and International Atomic Energy Agency Nuclear Fusion
Nucl. Fusion **53** (2013) 083007 (12pp) doi:10.1088/0029-5515/53/8/083007

Electron-scale turbulence spectra and plasma thermal transport responding to continuous $E \times B$ shear ramp-up in a spherical tokamak

Y. Ren[1], W. Guttenfelder[1], S.M. Kaye[1], E. Mazzucato[1], R.E. Bell[1], A. Diallo[1], C.W. Domier[2], B.P. LeBlanc[1], K.C. Lee[2], M. Podesta[1], D.R. Smith[3] and H. Yuh[4]

[1] Princeton Plasma Physics Laboratory, Princeton, NJ 08543, USA
[2] Department of Electrical and Computer Engineering, University of California at Davis, Davis, CA 95616, USA
[3] Department of Engineering Physics, University of Wisconsin-Madison, Madison, WI 53706, USA
[4] Nova Photonics, Inc., Princeton, NJ 08540, USA

Received 31 December 2012, accepted for publication 10 June 2013
Published 8 July 2013
Online at stacks.iop.org/NF/53/083007

Abstract
Microturbulence is considered to be a major candidate in driving anomalous transport in fusion plasmas, and the equilibrium $E \times B$ shear generated by externally driven flow can be a powerful tool to control microturbulence in future fusion devices such as FNSF and ITER. Here we present the first observation of the change in electron-scale turbulence wavenumber spectrum (measured by a high-k scattering system) and thermal transport responding to continuous $E \times B$ shear ramp-up in an NSTX centre-stack limited and neutral beam injection-heated L-mode plasma. It is found that while linear stability analysis shows that the maximum electron temperature gradient mode linear growth rate far exceeds the observed $E \times B$ shearing rate in the measurement region of the high-k scattering system, the unstable ion temperature gradient (ITG) modes are susceptible to $E \times B$ shear stabilization. We observed that as the $E \times B$ shearing rate is continuously ramped up in the high-k measurement region, the ratio between the $E \times B$ shearing rate and maximum ITG mode growth rate continuously increases (from about 0.2 to 0.7) and the maximum power of the measured electron-scale turbulence wavenumber spectra decreases. Meanwhile, electron and ion thermal transport is also reduced in the outer half of the plasmas as long as magnetohydrodynamic activities are not important and the L-mode plasmas eventually reach H-mode-like confinement. Linear and nonlinear gyrokinetic simulations are presented to address the experimental observations.

(Some figures may appear in colour only in the online journal)

1. Introduction

Microturbulence is considered to be a major candidate in driving anomalous transport in fusion plasmas [1] and the ion temperature gradient (ITG) mode [2], trapped electron mode (TEM) [3], electron temperature gradient (ETG) mode [4] and micro-tearing mode [5, 6] are well-known instabilities which could drive microturbulence there. One important aspect of controlled magnetic fusion research is to understand the operational micro-instabilities in fusion plasma and their operational regimes and thus to control them in future fusion devices, e.g. Fusion Nuclear Science Facility (FNSF) [7] and ITER. An important tool for controlling microturbulence in these devices is the equilibrium $E \times B$ shear generated by externally driven (or intrinsically generated) plasma flow [8]. It was pointed out that $E \times B$ shear affects microturbulence and associated turbulent transport both linearly and nonlinearly: change mode stability, e.g. enhance damping by coupling to stable modes; change the relative phase between fluctuation quantities, e.g. density fluctuation and radial velocity fluctuations; reduce fluctuation amplitude. The most physical way to determine the effect of $E \times B$ shear on turbulence is to compare $E \times B$ shearing rate, $\omega_{E\times B}$, with turbulence decorrelation rate as pointed out in [9]. However, the turbulence decorrelation rate is usually unknown, and a rule of thumb is that turbulence is significantly stabilized by $E \times B$ shear when the Hahm–Burrell $E \times B$ shearing rate [9], $\omega_{E\times B,\mathrm{HB}}$, is larger than the maximum linear growth rate of

a particular instability, $\gamma_{\max}$ [8]. A quantitative numerical study of $E \times B$ shear effects on turbulence and transport was reported in [10], where extensive linear and nonlinear gyrokinetic simulations were used to determine the amount of $\omega_{E\times B}$ needed for quenching thermal transport driven by a specific kind of plasma turbulence. In particular, the ion-scale turbulence (ITG/TEM) and the associated turbulent transport is found to be quenched if $\omega_{E\times B,\mathrm{WM}}/\gamma_{\max} \approx 1.41(A/3)^{0.6}/(\kappa/1.5)$, where $\omega_{E\times B,\mathrm{WM}}$ is the Waltz–Miller $E \times B$ shearing rate [11], $\gamma_{\max}$ is the maximum linear growth rate for a particular instability, A is the aspect ratio and κ is the elongation. In fact, experiments have shown that increase in $E \times B$ shear is correlated with the formation of H-mode edge transport and internal barriers and reduction in ion-scale turbulence [12, 13]. However, we note that in these cases, the $E \times B$ shear mainly comes from pressure gradient rather than plasma rotation. On the other hand, spherical tokamaks (STs) with tangential neutral beam heating typically have strong toroidal flow with Mach number approaching 1, and $E \times B$ shear can be dominated by the contribution from plasma rotation. Thus ion-scale turbulence is expected to be stabilized by $E \times B$ shear, which is supported by the observed neoclassical level of ion thermal transport in STs [14, 15]. Furthermore, $E \times B$ shear was also shown to suppress electron-scale turbulence when the $E \times B$ shearing rate is comparable to the maximum ETG linear growth rate [16], where electron-scale turbulence was measured by a high-k scattering system [17] on the National Spherical Torus eXperiment (NSTX) [18]. However, the change in spectral shape was not explored in [16] since only a single k measurement was available due to limitations in the scattering scheme and most importantly correlation with transport was not investigated.

In this paper, with much improved scattering schemes of this high-k scattering system, we present the first experimental observation of a progressive change in electron-scale turbulence wavenumber spectrum and thermal transport at the core–edge transition region of an NSTX centre-stack limited and neutral beam injection (NBI)-heated L-mode plasma ($r/a \sim 0.66$–0.78), as $E \times B$ shearing rate is continuously increased due to plasma toroidal velocity increase from NBI. We observed that as $E \times B$ shearing rate is continuously increased, the ratio between the $E \times B$ shearing rate and maximum ITG mode growth rate continuously increases and the maximum power of the measured electron-scale turbulence wavenumber spectra decreases. Meanwhile, both the electron and ion thermal transports are also reduced as long as MHD activities are not important and the L-mode plasmas eventually reach H-mode-like confinement. These observations are consistent with that some of the observed electron-scale turbulence is nonlinearly driven by ITG turbulence through nonlinear cascade [19] and/or ITG-driven background T_e gradient fluctuations [20] and its power decreases as ITG turbulence is progressively suppressed by $E \times B$ shear. We note that other mechanisms, e.g. nonlocality of turbulence [21] may also contribute. We found that heat fluxes predicted by local nonlinear ITG simulations at different radial locations can be larger or significantly smaller than the corresponding local experimental heat fluxes depending on the local $E \times B$ shearing rate, which indicates that global effects may have to be included in future simulations. Multi-scale/global gyrokinetic simulations are needed to further investigate the mechanisms behind the observed reduction in electron-scale turbulence.

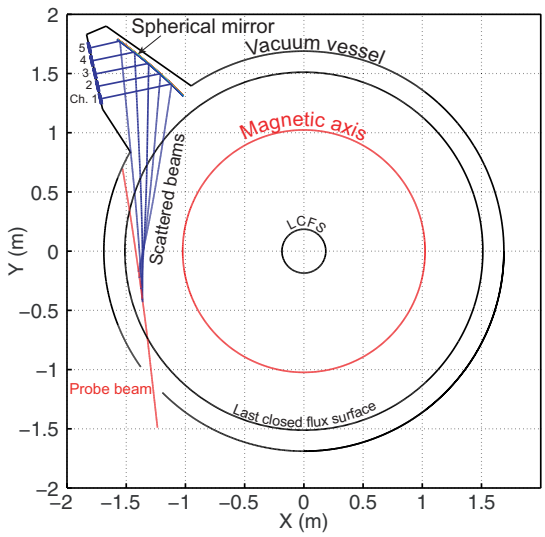

Figure 1. Schematic of the scattering configuration of the high-k scattering system used in the study presented in this paper. The probe beam and scattered beam trajectories are calculated using a ray-tracing code. Scattered light is reflected and focused by a spherical mirror onto five collection windows.

We organize this paper follows. In section 2, experimental apparatus is presented. Experimental observations are described in section 3, followed by comparisons with linear and nonlinear gyrokinetic simulations in section 4. Finally, we summarize and discuss the results in section 5.

2. Experimental apparatus

Figure 1 plots the scattering configuration of the high-k scattering system [17] used in this paper, including the probe beam and scattered beam trajectories calculated using a ray tracing code. The five receiving channels cover a wavenumber range of $5\,\mathrm{cm}^{-1} \lesssim k_\perp \lesssim 30\,\mathrm{cm}^{-1}$ with a resolution of about $1\,\mathrm{cm}^{-1}$, and five heterodyne receivers allow us to distinguish the wave propagation direction for each different wavenumber. The power response of each receiving channel was calibrated with a solid-state microwave source with known output power. We note that although the scattering signals are not absolutely calibrated to obtain actual density fluctuations, they are relatively calibrated across channels and are known to be proportional to density fluctuations (see [22, 23] for more details). Thus it is possible for us to compare relative wavenumber spectral power across different scattering channels and at different experimental time points. The frequency response of the scattering system is about 5 MHz. A radial resolution of $\triangle R \approx \pm 2$ cm, determined by the $1/e$ half width of the microwave beam power, is the unique feature of the scattering system. This is made possible by the tangential launching scheme along with the large toroidal curvature of NSTX due to its low aspect ratio which lead to a scattering volume much smaller than that from a simple overlapping of the probe and scattering beams [24]. This fine radial resolution allowed us to study the dependence of locally measured turbulence on local equilibrium quantities,

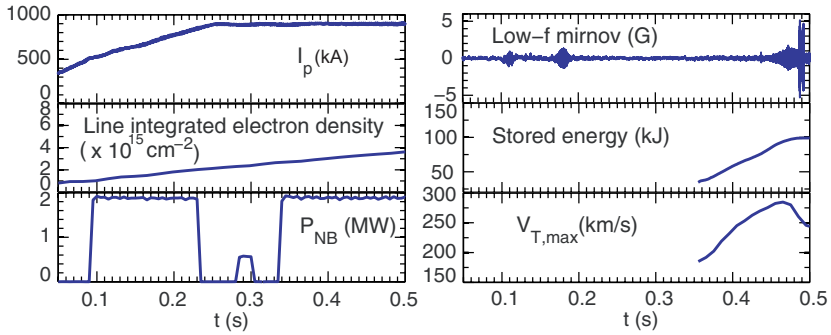

Figure 2. An overview of shot 141716 with time traces of plasma current, linear integrated electron density, neutral beam power (P_{NB}), low-f magnetic fluctuation, stored energy and maximum plasma toroidal flow velocity.

e.g. L_{T_e} [25] (electron temperature scale length), L_{n_e} [26, 27] (electron density scale length), collisionality [27], q (safety factor) and $\hat{s}$ (magnetic shear) [28]. Recent improvements in scattering scheme have significantly reduced stray radiation, which made it possible to obtain scattering signals from all five channels simultaneously, compared with at most three channels previously [23]. Newly implemented remote control capability allows between-shot adjustment of launching and receiving optics, which made it possible to optimize scattering configuration according to realized plasma equilibria. We note that due to the tangential launching scheme employed (see figure 1), the scattering system measures mostly radial wavenumber, k_{r}, and finite but smaller binormal wavenumber, k_θ, e.g. a range $k_{\mathrm{r}}\rho_{\mathrm{s}} \sim 5$–13 and a range $k_\theta\rho_{\mathrm{s}} \sim 2$–4 for the experiments presented in this paper, where ρ_{s} is the ion gyroradius with sound speed (the ρ_{s} is calculated with locally measured T_{e} and local magnetic field strength from equilibrium reconstruction). We note that as shown in figure 1, the scattered beam to channel 5 is partially blocked by the vacuum vessel and thus is not used in the following analysis. Furthermore, we would like to point out that since the scattering system measures mostly k_{r}, it does not capture the dominant k_θ spectral power predicted for ETG turbulence, e.g. see [29]. Here in this paper, the observed decrease in the measured k_{r} spectral power is used to evaluate the overall decrease in electron-scale turbulence intensity.

3. Experimental results

Observations on continuous $E \times B$ shear ramp-up were made in a set of centre-stack limited and NBI-heated L-mode plasmas. These plasmas have a toroidal field of 5.5 KG, a plasma current of 900 kA and a two-phase NBI with the first 2 MW NBI pulse from about 100 to 200 ms and the second 2 MW NBI pulse from about 350 ms to the end of discharges. During the second phase of NBI, plasma continuously spins up, which leads to a simultaneous increase in the $E \times B$ shearing rate in the outer half of the plasma ($r/a > 0.5$). Here in this paper, we present the observations from shot 141716 for which we have carried out extensive analysis. In this shot, the second 2 MW NBI pulse is re-injected from 335 ms after a first injection from 90 to 230 ms. With the presence of the 2 MW NBI pulses, ion temperature and plasma toroidal velocity are measured with charge exchange recombination spectroscopy (CHERS) measurements [30] and magnetic field pitch angle is measured by a motional stark effect (MSE) diagnostic [31]. Electron temperature and density are measured with multi-point Thomson scattering (MPTS) [32]. Plasma equilibrium is obtained using LRDFIT (LR circuit model with Data FITting capabilities) equilibrium reconstructions constrained by magnetic pitch angle measurements from the MSE diagnostic [33] and electron temperature iso-surfaces.

Figure 2 plots times traces of some relevant quantities for shot 141716. A two-phase NBI can be immediately seen in the figure. While the first phase of NBI is during the current ramp-up, the second phase of NBI is well into the flattop of plasma current. Line-integrated electron density shows continuous but slow increase through the shown time window. The low frequency Mirnov signal shows that no large MHD activity is present at the beginning of the second NBI pulse (from 330 to 450 ms) and that an $n = 1$ mode starts to grow at about $t = 450$ ms and saturates at about $t = 470$ ms. The stored energy (calculated using a time-dependent tokamak transport and data analysis code (TRANSP) [34]) is found to increase continuously from the beginning of the second NBI pulse and saturates at about the same time as the $n = 1$ MHD mode, which may not be coincident. It is also clear that the maximum plasma toroidal velocity, $V_{T,\mathrm{max}}$, also increases steadily after the second NBI pulse is initiated, indicating a continuous increase in $E \times B$ shear. We note that since we will be concentrating on the second phase of NBI and CHERS measurements are not available during the period between the two NBI pulses, stored energy and $V_{T,\mathrm{max}}$ are only shown for the time period of the second NBI pulse.

The electron and ion temperature, T_{e} and T_{i}, radial profiles are plotted in figures 3(a) and (b) at $t = 364$ and at $t = 448$ ms (corresponding to two exact MPTS time points). The high-k measurement region, the overall radial region covered by all channels with the centre of scattering location separated by $\lesssim$1 cm, is denoted by the shaded region in the figure from about $R = 139$–144 cm ($r/a \approx 0.66$–0.78). The H_{ITER98} [35] time trace shown in the inset in figure 3(a) shows about a factor of 2 increase in H_{ITER98} from $t = 350$ to 500 ms and we note that this increase is coincident with the increase in plasma toroidal flow velocity as shown in figure 2. We can see that both maximum T_{e} and T_{i} increase by about 50–100% as H_{ITER98} (and toroidal flow velocity) increases, and both T_{e} and T_{i} gradients also increase in the high-k measurement region. On the other hand, as we will show later, the gradient scale lengths remain relatively constant. We note that although the energy confinement of this L-mode plasma reaches that of the

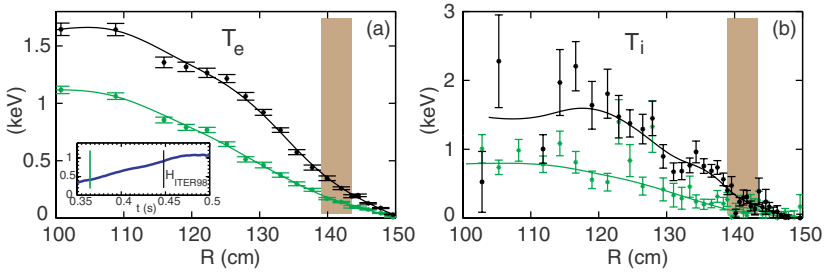

Figure 3. (*a*) Radial profiles of electron temperature at $t = 364$ and 448 ms; (*b*) radial profiles of ion temperature at $t = 364$ and 448 ms. The shaded regions in both panels denote the measuring of the high-k scattering system. Note that the inset in (*a*) shows the time trace of H_{ITER98} and the two vertical lines denote the time points used for (*a*) and (*b*).

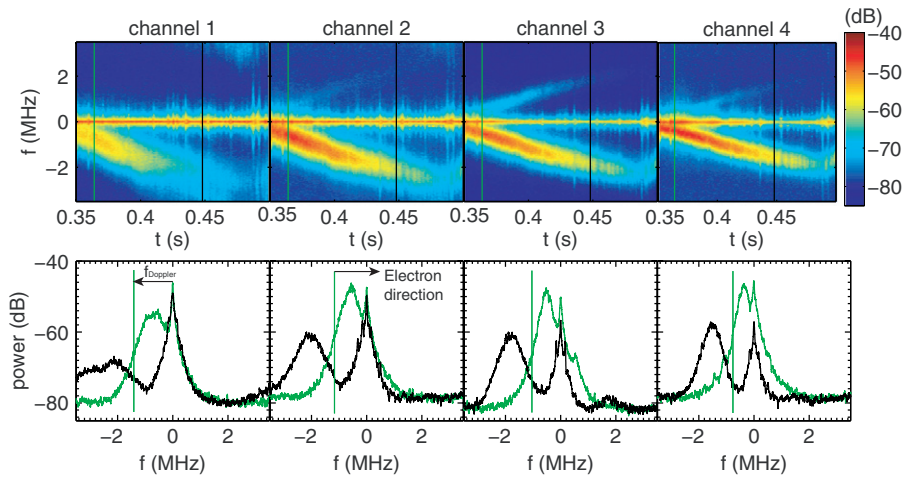

Figure 4. Upper panels: the spectrograms of four high-k channels during the second NBI pulse; lower panels: the frequency spectra at the two exact MPTS time points (the same as in figure 3) for four high-k channels. The two coloured lines in the upper panels denote time points used for plotting the lower panels with the same colour coding and the vertical lines in the lower panels denote the Doppler frequency shift, $f_{Doppler} = k_T V_T/2\pi$, for different channels at $t = 364$ ms (note that for clarity, only $f_{Doppler}$ at $t = 448$ ms is not shown). The electron direction is on the right-hand side of the vertical lines in the lower panels as indicated in the lower panel for channel 2.

H-mode plasmas in conventional tokamaks, no formation of an energy transport barrier has been observed, and as we will show later, thermal transport is reduced significantly in the outer half of the plasmas which is consistent with the increased $E \times B$ shear there.

Next we would like to show how measured electron-scale turbulence changes in the time range of interest ($t \sim 360$–480 ms). The upper panels of figure 4 show the spectrograms of the scattered signals from $t = 350$ to 500 ms (during which the plasma is spinning up), where the two exact MPTS time points, i.e. $t = 364$ and 448 ms, are denoted by two coloured lines in each panel. The lower panels show the frequency spectra at the above two time points for each of the four high-k channels. The wavenumbers measured by the four channels correspond to $k_\perp \rho_s$ of 8–10, 6–8, 4–6 and 2–4 from channels 1 to 4 at $t = 364$ ms. At $t = 448$ ms, because of the increase in T_e and density gradient, ρ_s and the wavenumber measured by each channel become larger, corresponding to $k_\perp \rho_s$ of 13–15, 10–12, 7–9 and 4–6 from channels 1 to 4, respectively. For each channel, the signal from collective scattering of microwave by electron density fluctuations manifests as spectral peaks at negative frequencies, which corresponds to wave propagation in the ion diamagnetic drift direction in the laboratory frame (lab frame). However, each channel has a Doppler frequency shift ($f_{Doppler} = k_T V_T/2\pi$, k_T is the toroidal wavenumber from ray tracing (see figure 1 for example) and V_T is the plasma toroidal flow velocity from CHERS measurement) denoted by vertical lines in the lower panels of figure 4. We note that the toroidal flow in the high-k measurement region is dominated by $E \times B$ flow and diamagnetic flow is small due to small pressure gradient. After subtracting the Doppler frequency shift, channels 1 to 4 show that the wave propagating direction is in the electron diamagnetic direction which is on the right-hand side of the vertical lines (only $f_{Doppler}$ at $t = 364$ ms is shown but conclusion is the same for $t = 448$ ms), and thus the propagation direction is in the electron direction. We also note that the large symmetric central peaks at $f = 0$ are due to the spurious reflections of the probing microwave beam. Large frequency separation of the scattering signals from the central peaks ensures accurate measurements of scattered microwave power. From figure 4, it can be immediately seen that the measured fluctuations in all channels show continuous increase in lab-frame fluctuation frequency, consistent with a Doppler frequency shift resulting from plasma spinning up. Furthermore, it is also clear that the fluctuation intensity denoted by colour in the spectrograms shows gradual decrease as the lab-frame mode frequency increases (a quantitative evaluation of the decrease can by seen in the lower panels). Having shown the frequency spectra, we show the change

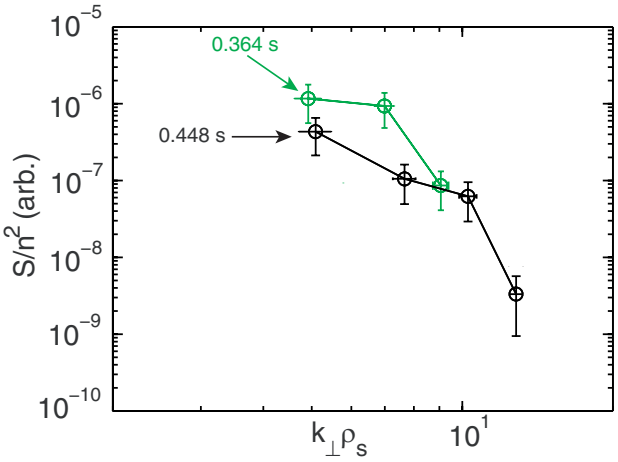

Figure 5. The $k_\perp$ spectra at the two MPTS time points (S is the spectral density).

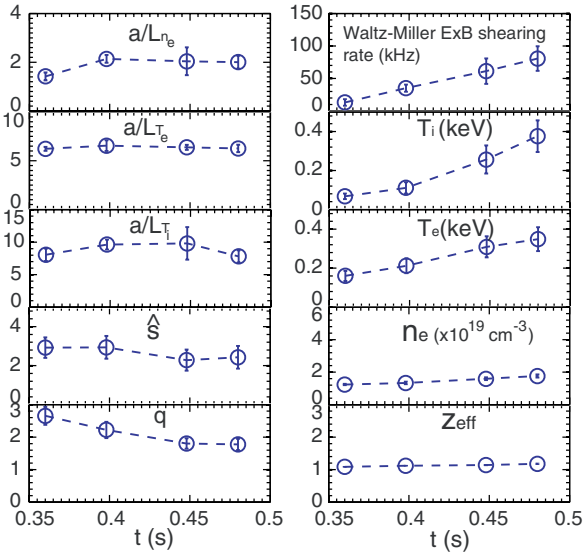

Figure 6. Ten relevant equilibrium quantities at $t = 364$, 398, 448 and 482 ms averaged in the high-k measuring region. Note that all inverse gradient scale lengths are normalized to a, the half width of the last closed flux surface at mid-plane.

in wavenumber spectra in figure 5, where the perpendicular wavenumber ($k_\perp$) spectra of normalized density fluctuation in arbitrary unit are plotted for the two MPTS time points. The figure clearly shows that fluctuation power at lowest measured wavenumber, $k\rho_s \sim 4$, decreases by about a factor of 2 and there is about a factor of 5 decrease in fluctuation power at $k\rho_s \sim 6$. It is interesting to note that the $k_\perp$ spectrum of $k\rho_s \gtrsim 10$ at $t = 448$ ms has a spectral slope similar to that of the $k_\perp$ spectrum of $k\rho_s > 6$ at $t = 364$ ms. We note that channel 4 is not used for $t = 364$ ms, since its scattering location is separated more than 2 cm from those of channels 1–3.

Here we would like to demonstrate that $E \times B$ shearing rate has the largest change in the high-k measurement region. Figure 6 plots ten relevant equilibrium quantities for four MPTS time points, $t = 364$, 398, 448 and 482 ms. Two more time points are added in addition to those used in previous figures in order show the temporal evolution of the equilibrium quantities. The error bars in the figure represent profile variations in the high-k measurement regions. It can be immediately seen that $E \times B$ shearing rate has the largest increase, about a factor of 5, from $t = 364$ to 482 ms. The $E \times B$ shearing rate shown is calculated with the Waltz–Miller definition [11]. Note the Waltz–Miller $E \times B$ shearing rate is about five times smaller than that calculated using Hahm–Burrell definition [9] and this will be shown in figure 7. Both T_i and T_e have substantial increase in correlation with the $E \times B$ shearing rate, consistent with the the change in T_i and T_e profiles and the confinement improvement shown in figure 3. It is also clear that the electron density, n_e, and effective ion charge, Z_{eff}, show small temporal variation. Other dimensionless quantities also show much smaller changes than $E \times B$ shearing rate. All normalized inverse gradient scale lengths for electron density (a/L_{n_e}), electron temperature (a/L_{T_e}) and ion temperature (a/L_{T_i}) have $\lesssim$40% variation. Furthermore, $\hat{s}$ and q change less than 30% through the time. It is no doubt that although small, the change in these dimensionless quantities may quantitatively change the growth of underlying instability, especially for a/L_{T_e} and a/L_{T_i} since they represent the amount of free energy to drive instabilities. Nevertheless, these effects are taken into account in the next section where we explore instabilities operating in this parametric regime.

We have shown in figure 6 that $E \times B$ shearing rate increases substantially through time in the high-k measurement region. Of course, this increase is not limited to the high-k measurement region. Figures 7(a) and (b) plot the radial profiles of $E \times B$ shearing rate using both the Waltz–Miller definition [11] and the Hahm–Burrell definition [9] (radial electric field from TRANSP analysis [34]). It is clear that $E \times B$ shearing rate increases are at outer half of the plasma, $r \gtrsim 130$ cm ($r/a \gtrsim 0.5$), from $t = 364$ to 448 ms. We note that the $E \times B$ shearing rate increase in this time period is correlated with the increase in $V_{T,\max}$ as shown in figure 2. From $t = 448$ to 482 ms, the region of $E \times B$ shearing rate increase moves further out to $r \gtrsim 139$ cm ($r/a \gtrsim 0.7$). It can been seen from figure 2 that $V_{T,\max}$ saturates and starts to decrease in this time period, and the increase in $E \times B$ shearing rate is due to change in the toroidal flow profile, most likely due to momentum transport from the $n = 1$ MHD mode. We also note that $E \times B$ shearing rate has large radial variation especially at $t = 448$ and 482 ms, e.g. $\gtrsim$ a factor of 2 variation in the high-k measurement region, which indicates that global effects may be important in modelling plasma thermal transport with gyrokinetic simulations. However, as a first step in interpreting experimental observations, we will focus on local gyrokinetic simulations in this paper (see next section).

The changes in plasma thermal transport from the TRANSP analysis are shown in figures 7(c) and (d). Figures 7(c) and (d) plot the radial profiles of ion thermal diffusivity, χ_i, and electron thermal diffusivity, χ_e, at $t = 364$, 398, 448 and 482 ms, respectively. (We note that the uncertainty in χ_i and χ_e in figures 7(c) and (d) is mainly due to uncertainties in ohmic heating and measured kinetic profiles). Note that for comparison, in figure 7(c) the radial profile of neoclassical ion thermal diffusivity, $\chi_{i,NC}$, at $t = 448$ ms is also shown. Figures 7(c) and (d) clearly show about a factor of 5 drop in χ_i and a factor of 3 drop in χ_e in the high-k measurement region from $t = 364$ to 448 ms. In more detail, from $t = 364$ to

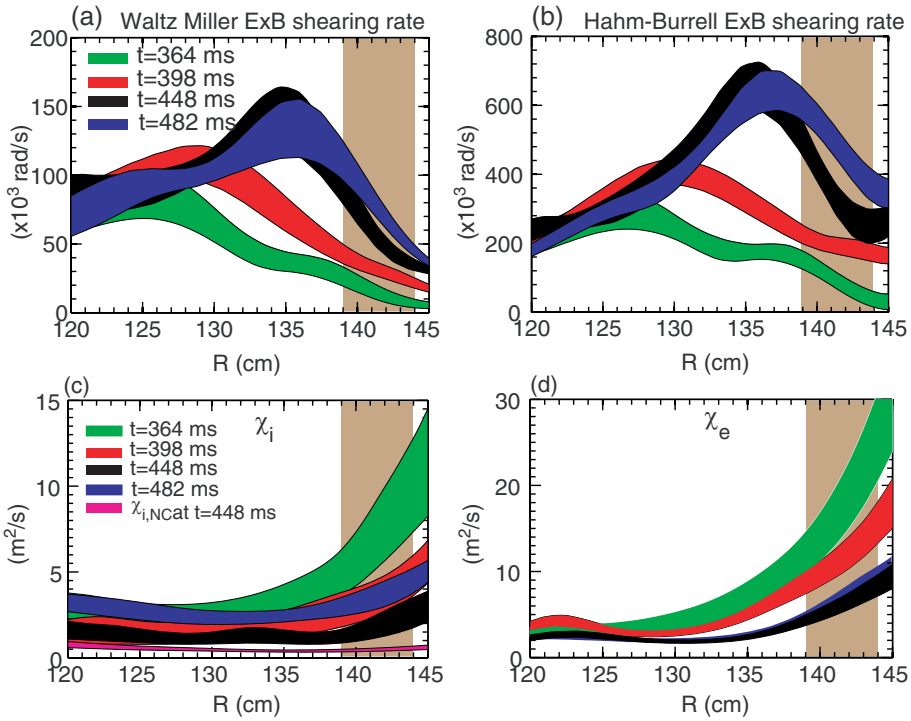

Figure 7. (*a*) Radial profiles of Waltz–Miller $E \times B$ shearing rate at $t = 364$ (green), 398 (red), 448 (black) and 482 (blue) ms; (*b*) radial profiles of Hahm–Burrell $E \times B$ shearing rate at the same time points and with the same colour coding as in (*a*); (*c*) radial profiles of ion thermal diffusivity, χ_i, at at the same time points and with the same colour coding as in (*a*) and radial profile of neoclassical ion thermal diffusivity at $t = 448$ ms (magenta); (*d*) radial profiles of electron thermal diffusivity, χ_e, at the same time points with the same colour coding as in (*a*). Note that the vertical width of the coloured bands denotes the experimental uncertainty. The width of rectangular shaded region denotes the high-k measurement region.

398 ms, χ_i decreases by about 50% and χ_e decreases by about 35% in the high-k measurement region, and a decrease in χ_i and χ_e by about 50% occurs from $t = 398$ to 0.448 ms. Overall, reductions in χ_i and χ_e are seen at $r \gtrsim 130$ cm ($r/a \gtrsim 0.5$), coincident with where $E \times B$ shearing rate increases most as shown in figures 7(*a*) and (*b*). It is also clear that $\chi_{i,NC}$ at $t = 448$ ms is $\gtrsim 0.5\,m^2\,s^{-1}$ and is about four times smaller than χ_i at the same time in the high-k measurement region. Examining $\chi_{i,NC}$ and χ_i across the radius, we found that χ_i approaches two–three times of $\chi_{i,NC}$, which shows that even at its smallest value in this discharge χ_i is still anomalous. We note that χ_e remains strongly anomalous and the electron channel is always the dominant channel for heat loss from the plasma. We would like point out that χ_i becomes about twice larger at $t = 482$ ms than that at $t = 448$ ms and at the same time χ_e has slight increase for $r > 140$ cm. As we have pointed out in figure 2, an $n = 1$ MHD mode starts to grow at about $t = 450$ ms and saturates at $t = 470$ ms. Thus it is likely that this MHD mode could enhance both ion and electron thermal transport at $t = 482$ ms in addition to microturbulence. However, in this paper, our analysis will be concentrating on the MHD-free time period.

Finally, to learn further experimental characteristics of the observed turbulence and to determine whether the characteristics would change as equilibrium quantities change, here we explore the turbulence dispersion relation using our high-k scattering measurements. As we have shown in figure 4, the measured fluctuation frequency is Doppler-shifted due to plasma toroidal flow. Thus the plasma-frame angular

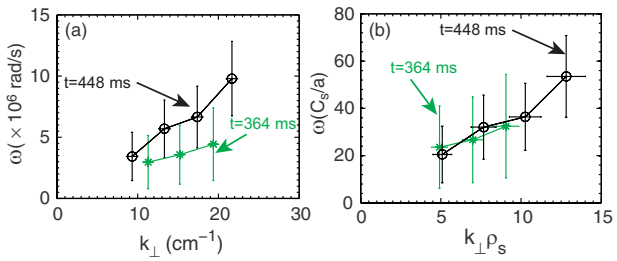

Figure 8. (*a*) Angular fluctuation frequency in the plasma frame as a function of $k_\perp$ at $t = 364$ (asterisks) and 448 ms (open circles); (*b*) normalized angular fluctuation frequency in the plasma frame as a function of $k_\perp \rho_s$ at $t = 364$ (asterisks) and 448 ms (open circles).

fluctuation frequency, ω, is calculated by subtracting Doppler frequency shift from the fluctuation frequency measured in the lab frame, ω_{Lab}, as $\omega = |\omega_{Lab} - k_T V_T|$, where $\omega_{Lab} = 2\pi \int f S(f)\,df / \int S(f)\,df$ ($S(f)$ is the frequency spectral power shown in figure 4). Figure 8(*a*) plots calculated ω as a function of $k_\perp$. We note that the uncertainties in ω come from uncertainties in k_T and V_T. It is clear that ω is larger for the same $k_\perp$ at $t = 448$ ms than at $t = 364$ ms, i.e. the phase velocity at $t = 448$ ms is larger. However, noting that T_e has also increased from $t = 364$ to 448 ms (see figure 6), we are motivated to normalize ω to C_s/a, where C_s is the sound speed, and $k_\perp$ to ρ_s^{-1}. The resulting normalized dispersion relation is plotted in figure 8(*b*), where the dispersion relations at $t = 364$ and 448 ms can be seen to overlap nicely with each other. This result shows that in dimensionless unit the

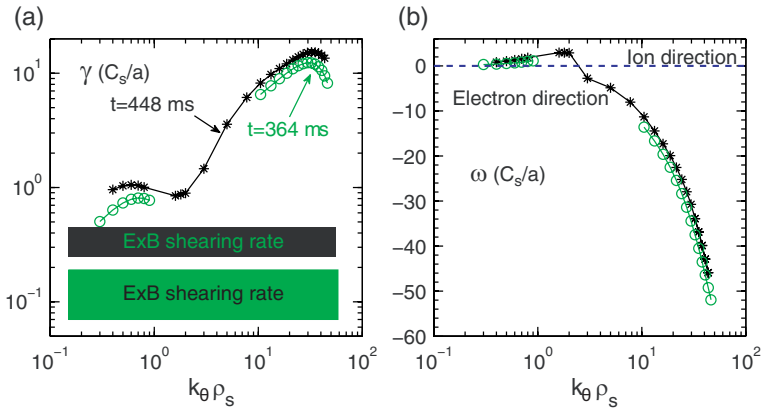

Figure 9. (*a*) Linear growth rate, γ, and (*b*) mode frequency, ω spectra at $t = 364$ ms (green open circles) and $t = 448$ ms (black asterisks) calculated with GS2 code at $R = 141$ cm ($r/a = 0.71$ about the centre of the high-k measurement region) using local Miller equilibrium. Note that modes with $\omega < 0$ propagate in the electron diamagnetic drift direction and $\omega > 0$ denotes the ion diamagnetic drift direction. $E \times B$ shearing rate calculated with the Waltz–Miller definition are also shown as coloured rectangles (green for $t = 364$ ms and black for $t = 448$ ms) with the vertical width denoting experimental uncertainty.

observed turbulence at the two time points is similar and is likely driven by the same microinstability. This observation is also supported by the previously mentioned similarity between the slope of the $k_\perp$ spectrum at $k\rho_s \gtrsim 10$ at $t = 448$ ms and that of the $k_\perp$ spectrum at $k\rho_s > 6$ at $t = 364$ ms (see figure 5).

4. Comparisons with gyrokinetic simulations

Linear gyrokinetic simulations were carried out using the experimental profiles for $t = 364$, 398, 448 and 482 ms. The linear stability analysis was performed with the GS2 gyrokinetic code [36]. GS2 is an initial value gyrokinetic code which, in its linear mode, finds the fastest growing mode for a given pair of poloidal and radial wavenumbers (radial wavenumber was set to zero to find the most unstable modes). Nonlinear simulations were performed with the Eulerian gyrokinetic code GYRO [37, 38]. Since nonlinear simulations are more expensive, we focus on the time point of $t = 448$ ms when the plasma reaches the highest confinement. A scan of $E \times B$ shearing rate based on experimental profiles at this time point was carried out. Here we present linear stability analysis in section 4.1 and nonlinear simulation results in section 4.2. We note that the linear simulations use local Miller equilibria [39], and the nonlinear simulations use the general equilibrium from a TRANSP analysis.

4.1. Linear stability analysis

The linear analysis was carried out from the ion scale ($k_y\rho_s \lesssim 1$) to the electron scale ($k_y\rho_e \sim 0.5$). Figure 9(*a*) shows that a wide k_θ range of linear modes is seen to be unstable with linear growth rate, γ, ranging from about 1 (C_s/a) at ion scale to $\gtrsim$10 (C_s/a) at both time points shown. The wave propagation direction seen in figure 9(*b*) gives the information on the nature of the modes. The ion-scale modes propagate in the ion diamagnetic direction and are identified as ITG modes. The electron-scale modes propagate in the electron direction and are identified as ETG modes. Comparing the linear growth rates with $E \times B$ shearing rates, we found that $E \times B$ shearing rates (in the unit of C_s) are comparable to ITG growth rates but are much smaller than those of ETG modes. Thus we expect $E \times B$ shear to affect ITG turbulence rather than ETG turbulence in this discharge. Furthermore, although the maximum growth rate of ITG modes at $t = 448$ ms is about 30% higher than $t = 364$ ms, the $E \times B$ shearing rate at $t = 448$ ms is about three times higher than that at $t = 364$ ms. Thus $E \times B$ shear could play a more important role in stabilizing ITG turbulence at $t = 448$ ms.

To model $E \times B$ shear effect on microturbulence, nonlinear gyrokinetic simulations are needed. However, here we use linear stability analysis to provide some initial assessment of the $E \times B$ shear effect in the experiment, motivated by studies on $\omega_{E\times B}$ and linear growth rate reported in [8, 10]. In figure 10(*a*), $\omega_{E\times B}/\gamma_{max}$ averaged in the high-k measurement region is plotted as a function of time, where both $\omega_{E\times B,HB}$ and $\omega_{E\times B,WM}$ are used, and γ_{max} is the maximum linear growth rate for ITG modes calculated with the GS2 code. We note that the gradual increase in $\omega_{E\times B}/\gamma_{max}$ from $t = 364$ to 448 ms is due to the increase in $\omega_{E\times B}$, while the faster increase in $\omega_{E\times B}/\gamma_{max}$ after $t = 448$ ms is due to both the increase in $\omega_{E\times B}$ and decrease in γ_{max}. Figure 10(*b*) shows the measured $k_\perp$ spectra at the time points used in figure 10(*a*). From $t = 364$ to 398 ms, the measured maximum spectral power (at $k_\perp\rho_s \approx 5$) decreases by about 40% while $\omega_{E\times B,WM}/\gamma_{max}$ increases from about 0.17 to 0.24. Meanwhile, the spectral power at larger wavenumbers ($k_\perp\rho_s \gtrsim 8$) has about a factor of 2 increase, and it appears that the slope of the spectra (at $k_\perp\rho_s \gtrsim 7$ for $t = 364$ ms and at $k_\perp\rho_s \gtrsim 8$ for $t = 398$ ms) is preserved. Larger decreases, about 60–80%, in spectral power at $k_\perp\rho_s \gtrsim 10$ occur while $\omega_{E\times B,WM}/\gamma_{max}$ approaches 0.4 at $t = 448$ ms and 0.7 at $t = 482$ ms. We note that from $t = 398$ to 448 ms the k spectra seem to preserve the shape and power at $k_\perp\rho_s \gtrsim 10$, but at $t = 482$ ms the spectral power at $k_\perp\rho_s \gtrsim 10$ also starts to drop. This overall decrease in spectral power with the large $\omega_{E\times B,WM}/\gamma_{max}$ ($\sim$0.7) at $t = 482$ ms is consistent with being close to the quenching threshold $\omega_{E\times B,WM} \approx 1.1 - 1.2\gamma_{max}$ calculated using a quenching rule, $\omega_{E\times B,WM}/\gamma_{max} \approx 1.41(A/3)^{0.6}/(\kappa/1.5)$ [10], with the local $A \approx 1.9$–2.1 and $\kappa \approx 1.5$ at $R = 141$ cm ($r/a = 0.71$). However, we note that this quenching rule was derived in the

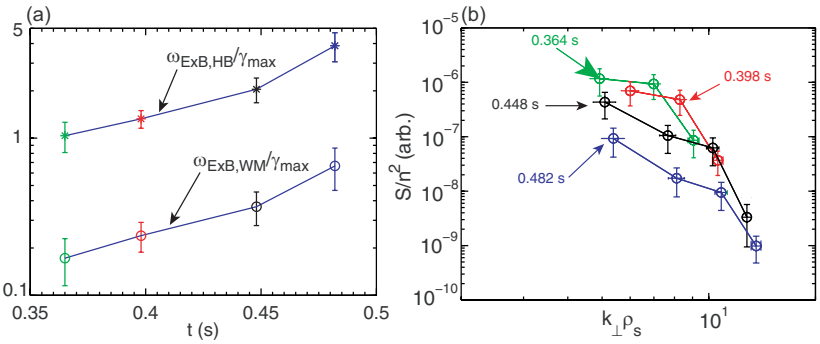

Figure 10. (*a*) The ratio between the $E \times B$ shearing rate and maximum linear growth rate of ITG modes (both the Hahm–Burrell and Waltz–Miller shearing rates are shown); (*b*) $k_\perp$ spectra in arbitrary unit at the four time points shown in (*a*).

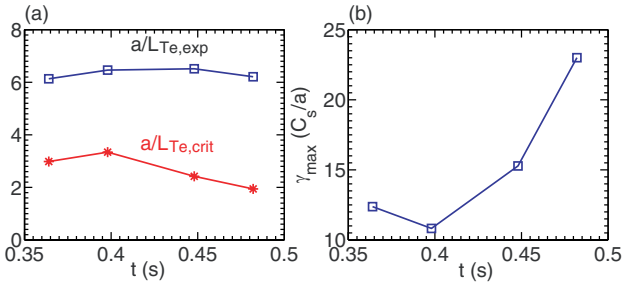

Figure 11. (*a*) Normalized inverse T_e gradient scale length (open squares), $a/L_{T_e,\mathrm{exp}}$, and calculated normalized ETG critical inverse gradient scale length (asterisks), $a/L_{T_e,\mathrm{crit}}$, using the GS2 code in the time period of interest from $t = 364$ to 482 ms; (*b*) maximum ETG linear growth rate, $\gamma_{\max}$, in the time period of interest.

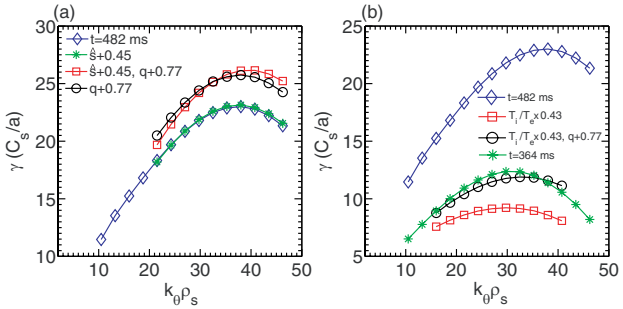

Figure 12. (*a*) ETG linear growth rate spectra for (1) $t = 482$ ms (open diamonds), (2) $\hat{s} + 0.45$ (asterisks), (3) $\hat{s} + 0.45$, $q + 0.77$ (open squares) and (4) $q + 0.77$ (open circles); (*b*) ETG linear growth rate spectra for (1) $t = 482$ ms (open diamonds), (2) $T_i/T_e \times 0.43$ (open square), (3) $T_i/T_e \times 0.43$, $q + 0.77$ (open circle) and (4) $t = 364$ ms (asterisks). Note that the specified changes in $\hat{s}$, q and T_i/T_e are relative to the values at $t = 482$ ms and are made to match the values at $t = 364$ ms.

local, electrostatic, collisionless limit using systematic scans around the GA standard case parameters with Miller local equilibrium model, and thus the needed $E \times B$ shear for quenching thermal transport for this NSTX L-mode plasmas has to be investigated with nonlinear gyrokinetic simulations which will be presented in section 4.2. Furthermore, we would like to point out that the changes in $\omega_{E\times B,\mathrm{WM}}/\gamma_{\max}$ shown in figure 10(*a*), i.e. about 40% increase from $t = 364$ to 398 ms and about 50% from $t = 0.398$ to 0.448 ms, correlates well with the change in χ_i and χ_e in the high-k measurement region shown in figures 7(*c*) and (*d*), i.e. decrease in χ_i by about 50% and χ_e by about 35% from $t = 364$ to 398 ms and another decrease in χ_i and χ_e by about 50% occurs from $t = 398$ to 448 ms. On the other hand, since the maximum ETG growth rate in the high-k measurement region (see figure 9) is much larger than the experimental $E \times B$ shearing rate ((0.1–0.4)C_s/a), ETG turbulence is unlikely to be affected by the experimental $E \times B$ shear. However, as we have shown in figure 10(*b*), electron-scale turbulence indeed decreases as $E \times B$ shear is increased. On the other hand, it is still possible that the change in equilibrium quantities as seen in figure 6 may lead to smaller ETG mode growth rate that could explain the observed reduction in electron-scale turbulence. In contrast, it is shown next that ETG mode is actually more unstable at $t = 482$ ms than at $t = 364$ ms, and the mechanism behind this trend is also presented below.

Figure 11(*a*) plots the normalized measured inverse T_e scale length, $a/L_{T_e,\mathrm{exp}}$ and the normalized critical inverse T_e scale length for ETG modes, $a/L_{T_e,\mathrm{crit}}$, at $R = 141$ cm (the centre of the high-k measurement region) in the time period of interest (calculated with the GS2 code). It can be seen in the figure that although the $a/L_{T_e,\mathrm{exp}}$ only varies between 6.1 and 6.4 from $t = 364$ to 482 ms, the $a/L_{T_e,\mathrm{crit}}$ decreases from about 3 to 2 during the same time period. Here a is used to normalize the measured and calculated inverse T_e scale lengths as used in the GS2 calculations. We note that the variation of a in the time period of interest is less than one per cent and thus it only makes negligible contributions to the temporal variations of $a/L_{T_e,\mathrm{exp}}$ and $a/L_{T_e,\mathrm{crit}}$ seen in figure 11(*a*). Thus ETG modes are expected to be more unstable at $t = 482$ ms than at 364 ms, and this trend can be clearly seen in figure 11(*b*) where the maximum ETG linear growth rate, $\gamma_{\max}$, increases from about 12.5 C_s/a at $t = 364$ ms to about 23 C_s/a at $t = 482$ ms. We note that the maximum ETG linear growth rates shown in figure 11(*b*) are calculated using all local equilibrium quantities at each time point.

In figure 12 we explore the mechanism behind this larger increase of ETG linear growth rates by varying different dimensionless quantities with others fixed. In particular, the effects of magnetic shear, q and T_i/T_e on linear growth rate are evaluated since they vary most during the time period of interest as shown in figure 6. In figure 12(*a*), magnetic shear, $\hat{s}$ and q are varied individually and also together (to match the values at $t = 364$ ms) with other equilibrium quantities fixed to the values at $t = 482$ ms. It can be seen that magnetic shear

has only small effects on linear growth rate, and on the other hand, increasing q by 0.77 (either with or without increasing $\hat{s}$) significantly increases the linear growth rate, γ, over the whole range of evaluated $k_\theta \rho_s$. However, the increase in γ due to the variation in q is not consistent with the decrease in γ from $t = 482$ to 364 ms (see figure 11(b)), and other equilibrium quantities must be responsible. In figure 12(b), T_i/T_e is varied to match the value at $t = 364$ ms with other equilibrium quantities fixed to the corresponding values $t = 482$ ms and this variation in T_i/T_e leads to a significant reduction in γ, which is now even smaller than the γ calculated for $t = 364$ ms. It is also seen in figure 12(b) that increasing q by 0.77 together with the above change in T_i/T_e leads to linear growth rates similar to those calculated for $t = 364$ ms. Note that this increase in γ with variations in both q and T_i/T_e compared with the γ from varying T_i/T_e alone is consistent with the observation in figure 12(a) that larger q leads to larger γ. From the above observations, we would like to conclude that it is the changes in q and T_i/T_e which lead to the large increase in the maximum γ shown in figure 11(b).

In summary, it is found that the change in linear growth rates of ETG modes due to the variation in equilibrium quantities alone does not likely explain the observed reduction in electron-scale turbulence seen in figure 10(b). Thus we expect additional nonlinear mechanism, i.e. $E \times B$ shear, should be considered to explain the observed reduction in electron-scale turbulence. One speculation is that some of the observed electron-scale turbulence is the result of a nonlinear cascade from ion-scale turbulence and the power of the electron-scale turbulence decreases as ion-scale turbulence is progressively suppressed by $E \times B$ shear. We note that other mechanisms may also be able to produce the observed reduction in electron-scale turbulence, e.g. reduced background T_e gradient fluctuations due to the $E \times B$ shear stabilization of ITG turbulence (therefore smaller drive for ETG modes) [20], and nonlocality of turbulence, e.g. strong $E \times B$ shear reducing ITG turbulence spreading [21]. We note that invoking $E \times B$ shear stabilization is important here since the trend in linear growth rates of ITG modes (i.e. linear growth rates of ITG modes at $t = 448$ ms larger than that at $t = 364$ ms and see figure 9(a)) is not consistent with the observed decrease in electron-scale turbulence (figure 10(b)). In order to fully investigate the above mechanisms, multi-scale and/or global gyrokinetic simulations are required. In particular, the nonlinear interactions between ITG and ETG turbulence, i.e. nonlinear cascade [19] and nonlinear T_e gradient drive [20], can be addressed by local multi-scale simulations which are planned in future work, and the nonlocality of turbulence should be investigated with global gyrokinetic simulations. However, we note that a global multi-scale simulation with NSTX geometry is unlikely to be feasible in the near future due to its need of enormous amount of computation power.

4.2. Comparison with nonlinear gyrokinetic simulations

Here we present the results from local nonlinear ITG gyrokinetic simulations based on experimental profiles at $t = 448$ ms. These local nonlinear simulations use general MHD equilibrium from LRDFIT equilibrium reconstructions and measured experimental profiles, kinetic electrons and ions

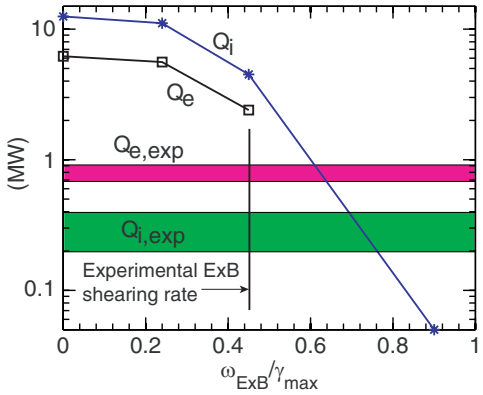

Figure 13. Electron and ion heat flux, Q_e (open square) and Q_i (asterisks), from a $E \times B$ shear scan as a function of $\omega_{E\times B}/\gamma_{max}$. The coloured horizontal bands denote the experimental electron and ion heat flux, $Q_{e,exp}$ (magenta) and $Q_{i,exp}$ (green), and the vertical width of the bands denotes the experimental uncertainty (mainly due to uncertainties in ohmic heating and measured kinetic profiles). Experimental $E \times B$ shearing rate is denoted by the vertical line.

with real mass ratio ($M/m_e = 3600$), collisions, shear and compressional magnetic perturbations (although we found that calculated transport is dominantly electrostatic), and toroidal flow and flow shear. All nonlinear simulations used a perpendicular box of $L_x \times L_y \approx 110 \times 110\rho_s$, 24 complex toroidal modes, 140 radial grid points, 8 energies, 12 pitch angles and 14 parallel mesh points ($\times 2$ signs of parallel velocity). We note that the nonlinear simulations presented here only resolve the ion-scale turbulence and the associated plasma transport. These simulations address the interesting observation presented in the paper that the observed L-mode plasmas developed H-mode-like confinement. With a $E \times B$ shearing rate scan (figure 13) and multiple local nonlinear simulations (figure 14), it is shown that the larger $E \times B$ shear can significantly affect both electron and ion thermal transport and is likely the mechanism underlying the confinement improvement. However, these ion-scale simulations do not address the electron- and ion-scale coupling which we think is needed for explaining the observed reduction in electron-scale turbulence. Further multi-scale and/or global gyrokinetic simulations will be carried out to address this issue and will be presented in a future paper.

Predicted electron and ion heat flux, Q_e and Q_i, from a numerical $E \times B$ shear scan (based on plasma equilibrium parameters at $r/a = 0.71$) are shown in figure 13, where Q_e and Q_i are plotted as a function of $\omega_{E\times B}/\gamma_{max}$. It is seen from figure 13 that large Q_e (~6 MW) and Q_i (~15 MW) are predicted with no $E \times B$ shear and thermal transport is reduced to $Q_e \sim 2$ MW and $Q_i \sim 6$ MW with experimental $E \times B$ shearing rate. Further increase in $E \times B$ shearing rate to the double of the experimental level leads to complete quenching of ion thermal transport and nonphysical electron thermal transport (transport from highest wavenumbers used in the simulation and thus not shown). We note that the nonphysical electron thermal transport only happens with the highest $E \times B$ shearing rate used in the scan (double of the experimental level) and is not present with experimental parameters with which the nonlinear simulations show well-behaved electron thermal transport spectrum, i.e. no electron thermal transport piling-up

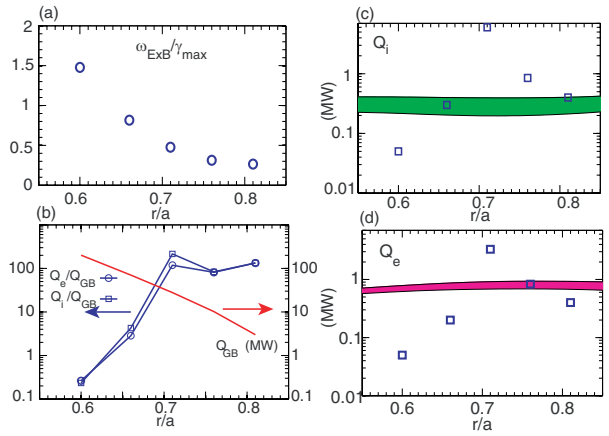

Figure 14. (*a*) $\omega_{E\times B}/\gamma_{\max}$ as a function of r/a; (*b*) predicted electron and ion heat flux normalized to the gyro-Bohm unit, Q_e/Q_{GB} (open circle) and Q_i/Q_{GB} (open square) and the gyro-Bohm unit, Q_{GB} (red line); (*c*) predicted (open squares) and experimental (coloured band) Q_i as a function of r/a; (*d*) predicted (open squares) and experimental (coloured band) Q_e as a function of r/a. The vertical width of the bands denotes the experimental uncertainty.

at the highest simulated wavenumbers. Thus, this $E \times B$ shear scan shown in figure 13 clearly demonstrates that increasing $E \times B$ shear can significantly reduce Q_e and Q_i driven by ITG turbulence and the critical $E \times B$ shearing rate for quenching of ITG-driven thermal transport is between one and two times of experimental $E \times B$ shearing rate, which corresponds to a critical $\omega_{E\times B}/\gamma_{\max}$ between 0.44 and 0.9. We note that this value is clearly lower than the quenching threshold of 1.1–1.2 estimated in section 4.1, and this is not surprising as we have discussed in section 4.1. We also compare predicted heat fluxes with experimental $Q_{e,exp}$ and $Q_{i,exp}$ in figure 13. It can be seen that with experimental $E \times B$ shearing rate, the numerical simulation clearly over-predicts electron and ion heat flux comparing with experiments, and furthermore, the simulation shows ion as the dominant channel of heat loss while in experiment, electron channel remains dominant. Of course, the predicted heat fluxes may be sensitive to ETG/ITG, which may reduce these discrepancies when we consider the measurement error in temperature gradients. As part of our future work, we will test this sensitivity by varying ETG/ITG. Furthermore, the lack of global effects (large ion gyroradius in NSTX and profile variation) in local gyrokinetic simulations may also lead to the above discrepancies. Indeed, in figure 7, about a factor of 2 variation of $E \times B$ shearing rate in the high-k measurement region (about $6\rho_i$ in width) can be seen.

Given the strong radial variation of $E \times B$ shearing rate seen in figure 7, we are motivated to carry out multiple local gyroinetic simulations to assess the effects of $E \times B$ shear at different radial locations around the high-k measurement region. We note that although this approach does not include the global effects, a large radial variation in predicted heat flux, if seen, would indicate the need to include global effects. In figure 14(*a*), we plot $\omega_{E\times B}/\gamma_{\max}$ as a function of r/a, and it can be immediately seen that $\omega_{E\times B}/\gamma_{\max}$ has a large radial variation about a factor of 5 from $r/a = 0.6$ to 0.81 which mostly comes from the radial variation of $E \times B$ shearing rate. In particular, $\omega_{E\times B}/\gamma_{\max}$ reaches about 1.5 at $r/a = 0.6$, and from what is observed in figure 13, we expect predicted heat flux is totally quenched at $r/a = 0.6$. It is also seen that $\omega_{E\times B}/\gamma_{\max}$ starts to saturate at $r/a > 0.7$ where we would expect predicted heat flux to saturate as well. In fact, what is shown in figure 14(*b*) agrees with both our expectations. Both normalized electron and ion heat fluxes, Q_e/Q_{GB} and Q_i/Q_{GB} ($Q_{GB} = \rho_s^2/a^2 n_e C_s T_e$ is the gyro-Bohm unit, where C_s is the sound the speed and n_e is the electron density), are at minimal at $r/a = 0.6$ in agreement with strong $E \times B$ shear stabilization and are saturated at ~100 level at $r/a > 0.7$ in agreement with reduced $E \times B$ shear effect and saturated $\omega_{E\times B}/\gamma_{\max}$. Figure 14(*b*) also plots the profile of Q_{GB} which demonstrates the strong $Q_{GB} \sim T_e^{5/2}$ dependence that decreases by about 2 orders of magnitude from $r/a = 0.6$ to 0.81. To compare with experimental results, the normalized electron and ion heat fluxes are multiplied with Q_{GB} and the resulting Q_i and Q_e profiles are shown in figures 14(*c*) and (*d*), respectively, together with their experimental counterparts (shown as the coloured bands). It is obvious from figures 14(*c*) and (*d*) that the predicted Q_i and Q_e profiles have large radial variations in contrast to the experimental profiles which are fairly flat. It is also seen that the simulation significantly under-predicts Q_i and Q_e at $r/a = 0.6$ comparing with experiment, which is consistent with the strong $E \times B$ shear present there as shown in figure 14(*a*). From $r/a = 0.6$ to 0.71, both predicted Q_i and Q_e increase by about 2 orders of magnitude, which is consistent with a reduction in $E \times B$ shear stabilization evident from the decrease in $\omega_{E\times B}/\gamma_{\max}$ in figure 14(*a*). Predicted Q_i and Q_e peak at $r/a = 0.71$ and are significantly larger than experimental values as already shown in figure 13. Furthermore, from figure 14(*b*), it can be seen that the order of magnitude decrease in predicted Q_i and Q_e from $r/a = 0.71$ to 0.81 is mostly due to the significant decrease in Q_{GB}, and the agreement with experimental Q_i and Q_e is within a factor of 2 at $r/a = 0.81$. Overall, we can conclude that the predicted Q_i and Q_e from local nonlinear ITG gyrokinetic simulations are consistent with the radial variation of $E \times B$ shearing rate, but we have both significant over- and under-prediction of heat fluxes in the evaluated region. As we have pointed out, this is the indication that global effects may be needed for explanation of the observation and we are actively pursuing global gyrokinetic simulations. Furthermore, in the strongly sheared region, e.g. around $r/a = 0.6$, high-k modes, i.e. ETG, may be important for electron thermal transport and nonlinear ETG simulation will be carried out to assess this. However, the inclusion of ETG modes does not help explaining the above observed discrepancy in ion heat flux.

5. Summary and discussions

In this paper, we have presented the first observation of the change in electron-scale turbulence wavenumber spectrum and thermal transport responding to continuous $E \times B$ shear ramp-up in an NSTX centre-stack limited and NBI-heated L-mode plasma, where in a time period of plasma spin-up the global energy confinement continues to increase and reaches the H-mode confinement of conventional tokamaks without formation of a transport barrier. During the same time period, the frequency spectra of electron-scale turbulence measured by the microwave scattering system clearly show an almost linear

increase in fluctuation frequency and a decrease in fluctuation power as the plasma toroidal flow speed increases. The former is consistent with the increase in Doppler frequency due to plasma spin-up, and the later indicates an interplay between shear flow and plasma turbulence. A correlation between shear flow and reduction in electron-scale turbulence is further supported by the observation of a factor 5 increase in $E \times B$ shearing rate in the high-k measurement region with much smaller change in n_e, Z_{eff} and other dimensionless quantities as shown in figure 6. Furthermore, both the electron and ion thermal transports are found to decrease in the outer half of the plasma coinciding with where $E \times B$ shear changes most, when MHD activities are small. This observation indicates that the responsible instability for thermal transport should be strongly affected by $E \times B$ shear. We have also investigated the dispersion relation of the observed turbulence by subtracting the Doppler frequency from measured fluctuation frequency to obtain fluctuation frequency in the plasma frame. The most interesting feature we identified is that the normalized dispersion relation ($\omega/(C_s/a)$ versus $k_\perp \rho_s$) is self-similar even with electron-scale turbulence spectral power significantly reduced, which indicates that the nature of the turbulence remains the same. We would like to point out that this self-similarity is consistent with the small change in dimensionless quantities, as shown in figure 6.

We took an initial approach by comparing $E \times B$ shearing rate and maximum growth rates of unstable ITG and ETG modes (calculated by GS2 code [36]), and this approach was shown to reasonably represent the nonlinear $E \times B$ shear stabilization effect on turbulence [10]. We found that while linear stability analysis shows that the maximum ETG mode linear growth rate far exceeds the observed $E \times B$ shearing rate in the measurement region of the high-k scattering system, the unstable ITG modes are susceptible to $E \times B$ shear stabilization. As $E \times B$ shearing rate is continuously ramped up in the high-k measurement region, the ratio between the $E \times B$ shearing rate and maximum ITG mode growth rate continuously increases (from about 0.2 to 0.7) but does not reach the quenching threshold predicted using the result from [10], and the fact that the measured ion thermal diffusivity, at its minimum, is still two- to three-times the neoclassical value is consistent with that ITG turbulence is stabilized but not completely suppressed by $E \times B$ shear. At the same time the maximum power of measured electron-scale turbulence $k_\perp$ spectra decreases. However, we have pointed out that the observed $E \times B$ shearing rate is close to ITG growth rate but is much smaller than ETG growth rate, and thus the $E \times B$ shear should not affect ETG turbulence as much as it does to ITG turbulence. Further analysis of ETG linear stability shows that ETG linear growth rates increase in the time period of interest, i.e. $t = 364$ to 482 ms, and the change in ETG linear growth rate is found to mainly result from the equilibrium changes in q and T_i/T_e with T_i/T_e as the dominant factor leading to the increase in ETG linear growth rates. This increase in ETG linear growth rate from $t = 364$ to 482 ms excludes a simple explaining of the observed reduction in electron-scale turbulence based on linear analysis. Thus other mechanisms are needed to explain the observation. Possible mechanisms may involve nonlinear couplings between ion- and electron-scale turbulence: some of the electron-scale turbulence is a result of nonlinear cascade from ITG turbulence [19] or ETG turbulence is nonlinearly excited by ITG turbulence [20], and once ITG turbulence is stabilized by $E \times B$ shear, the resulting electron-scale turbulence is also reduced. Other mechanisms may also contribute, e.g. nonlocality of turbulence, e.g. strong $E \times B$ shear reducing ITG turbulence spreading [21]. We have pointed out that multi-scale/global nonlinear gyrokinetic simulations are needed to investigate the above mechanisms. Local multi-scale nonlinear gyrokinetic simulations and global nonlinear simulations are planned to be carried out in the future work to address proposed mechanisms.

Local nonlinear gyrokinetic simulations were performed to quantitatively characterize the $E \times B$ shear effect on ITG turbulence. An $E \times B$ shear scan at a fixed radius of $r/a = 0.71$ shows that $E \times B$ shear can significantly reduce both electron and ion heat fluxes, although the simulation still over-predicts heat fluxes with experimental $E \times B$ shearing rate. It is also found that $E \times B$ shearing rate between one- and two-times of the experimental value is needed to completely quench ion thermal transport. Multiple local simulations were carried out around the high-k measurement region, motivated by the observation of large radial variation of $E \times B$ shearing rate. It is found that the radial variation of predicted Q_i/Q_{GB} and Q_e/Q_{GB} follows nicely what we have expected from the radial variation of $E \times B$ shearing rate: strong quenching of thermal transport around $r/a = 0.6$ with strong $E \times B$ shear and much increased and saturated thermal transport at $r/a > 0.71$ where $E \times B$ shearing rate is reduced and levels off. Comparison with experimental values shows significant under-prediction of thermal transport around $r/a = 0.6$, significant over-prediction around $r/a = 0.71$ and within-a-factor-of-2 agreement with experiment around $r/a = 0.81$. We have pointed out that this strong radial variation of predicted thermal transport level is associated with the large radial variation of $E \times B$ shear and Q_{GB} and indicates the need to include global effects in future numerical simulations. In addition, as we have pointed out, we will also investigate the sensitivity of these results on electron/ion temperature gradient in our future work. Furthermore, high-k turbulence, i.e. ETG, may also contribute to electron thermal transport. This is reasonable since $Q_{e,exp} > Q_{i,exp}$ seen in figure 13 shows that electrons are the dominant transport channel. Thus, we are planning to carry out nonlinear ETG simulations where $E \times B$ shear is strong enough to suppress ion-scale turbulence, e.g. around $r/a = 0.6$. However, at other radial locations, e.g. around $r/a = 0.71$, multiple-scale simulations will be needed to fully investigate the contribution to thermal transport from both electron- and ion-scale turbulence. Multi-scale simulations, as we have discussed, are also essential to assess the speculated nonlinear couplings [19, 20] between ion-scale and electron-scale turbulence and to quantitatively compare turbulence characteristics, e.g. dispersion relation and wavenumber spectra, with experiments.

Acknowledgments

The author would like to thank the NSTX Team for the excellent technical support for this work. This work was supported by the US Department of Energy contracts No DE-AC02-09CH11466, No DE-FG03-95ER54295 and No DE-FG03-99ER54518.

References

[1] Tang W. 1978 *Nucl. Fusion* **18** 1089
[2] Coppi B. and Pegoraro F. 1977 *Nucl. Fusion* **17** 969
[3] Kadomtsev B. and Pogutse O. 1971 *Nucl. Fusion* **11** 67
[4] Lee Y.C. *et al* 1987 *Phys. Fluids* **30** 1331
[5] Hazeltine R.D. and Strauss H.R. 1976 *Phys. Rev. Lett.* **37** 102
[6] Drake J.F. *et al* 1980 *Phys. Rev. Lett.* **44** 994
[7] Menard J.E. *et al* 2011 *Nucl. Fusion* **51** 103014
[8] Burrell K.H. 1997 *Phys. Plasmas* **4** 1499
[9] Hahm T.S. and Burrell K.H. 1995 *Phys. Plasmas* **2** 1648
[10] Kinsey J.E. *et al* 2007 *Phys. Plasmas* **14** 102306
[11] Waltz R.E. and Miller R.L. 1999 *Phys. Plasmas* **6** 4265
[12] Ritz C.P. *et al* 1990 *Phys. Rev. Lett.* **65** 2543
[13] Mazzucato E. *et al* 1996 *Phys. Rev. Lett.* **77** 3145
[14] Kaye S.M. *et al* 2007 *Nucl. Fusion* **47** 499
[15] Field A.R. *et al Proc. 20th Int. Conf. on Fusion Energy 2004 (Vilamoura, Portugal, 2004)* (Vienna: IAEA) CD-ROM file EX/P2-11 and www-naweb.iaea.org/napc/physics/fec/fec2004/datasets/index.html
[16] Smith D.R. *et al* 2009 *Phys. Rev. Lett.* **102** 225005
[17] Smith D.R. *et al* 2008 *Rev. Sci. Instrum.* **79** 123501
[18] Ono M. *et al* 2000 *Nucl. Fusion* **40** 557
[19] Kraichnan R.H. 1965 *Phys. Fluids* **8** 1385
[20] Jenko F. 2004 *J. Plasma Fusion Res. Ser.* **6** 11
[21] Wang W.X. *et al* 2007 *Phys. Plasmas* **14** 072306
[22] Mazzucato E. 1976 *Phys. Rev. Lett.* **36** 792
[23] Mazzucato E. *et al* 2009 *Nucl. Fusion* **49** 055001
[24] Mazzucato E. 2003 *Phys. Plasmas* **10** 753
[25] Mazzucato E. *et al* 2008 *Phys. Rev. Lett.* **101** 075001
[26] Ren Y. *et al* 2011 *Phys. Rev. Lett.* **106** 165005
[27] Ren Y. *et al* 2012 *Phys. Plasmas* **19** 056125
[28] Yuh H.Y. *et al* 2011 *Phys. Rev. Lett.* **106** 055003
[29] Guttenfelder W. and Candy J. 2011 *Phys. Plasmas* **18** 022506
[30] Bell R.E. 2006 *Rev. Sci. Instrum.* **77** 10E902
[31] Levinton F.M. *et al* 2007 *Phys. Plasmas* **14** 056119
[32] LeBlanc B.P. *et al* 2003 *Rev. Sci. Instrum.* **74** 1659
[33] Menard J.E. *et al* 2006 *Phys. Rev. Lett.* **97** 095002
[34] Hawryluk R.J. 1981 *Physics of Plasma Close to Thermonuclear Conditions* (New York: Pergamon)
[35] ITER Physics Basis 1999 *Nucl. Fusion* **39** 2175
[36] Kotschenreuther M. *et al* 1995 *Comput. Phys. Commun.* **88** 128
[37] Candy J. and Waltz R.E. 2003 *Phys. Rev. Lett.* **91** 045001
[38] Guttenfelder W. *et al* 2011 *Phys. Rev. Lett.* **106** 155004
[39] Miller R.L. *et al* 1998 *Phys. Plasmas* **5** 973